Journal of Materials Chemistry A

Synthesis of MoS2 from [Mo3S7(S2CNEt2)3]I for Enhancing Photoelectrochemical Performance and Stability of Cu2O Photocathode Toward Efficient Solar Water Splitting

Journal:	*Journal of Materials Chemistry A*
Manuscript ID	TA-ART-02-2018-001771.R1
Article Type:	Paper
Date Submitted by the Author:	24-Apr-2018
Complete List of Authors:	Shinde, Pravin ; The University of alabama, Department of Chemistry Fontenot, Patricia ; Tulane University, Chemistry Donahue, James; Tulane University, Department of Chemistry Waters, joseph; The University of Alabama Kung, Patrick; The University of Alabama McNamara, Louis; University of Mississippi, Chemistry & Biochemistry Hammer, Nathan; University of Mississippi, Chemistry & Biochemistry Gupta, Arunava; University of Alabama, Chemistry + MINT center pan, shanlin; The University of Alabama, Department of Chemistry

Journal Name

ARTICLE

Synthesis of MoS_2 from $[Mo_3S_7(S_2CNEt_2)_3]I$ for Enhancing Photoelectrochemical Performance and Stability of Cu_2O Photocathode Toward Efficient Solar Water Splitting

Received 00th January 20xx,
Accepted 00th January 20xx

DOI: 10.1039/x0xx00000x

www.rsc.org/

P. S. Shinde,[ab] P. R. Fontenot,[c] J. P. Donahue,[c] J. L. Waters,[bd] P. Kung,[bd] L. E. McNamara,[e] N. I. Hammer,[e] A. Gupta[abf] and S. Pan*[ab]

Cu_2O is a typical *p*-type semiconductor that can efficiently absorb visible light and has a high absorption coefficient due to its narrow forbidden band. Thus, it finds potential applications in solar energy conversion and photocatalysis. However, Cu_2O photocathodes suffer from a major issue of chemical stability and sluggish proton reduction for splitting water using sunlight. We present here a facile method of coating a MoS_2 layer onto Cu_2O to significantly improve its stability and proton reduction efficiency. MoS_2 coating on top of Cu_2O is achieved from spin coating $[Mo_3S_7(S_2CNEt_2)_3]I$ combined with a thermal annealing process to obtain the optimal stoichiometry. MoS_2 films synthesized using this method show good prospects as both a protection layer and an electrocatalyst for hydrogen evolution reactions (HER) due to excellent stability and high electrocatalytic activity. The proton reduction performance of spin-coated MoS_2/FTO electrodes is studied to determine the optimal synthesis conditions using various derivatives of MoS_2 precursors. Our study suggests that the rate-limiting kinetic step of MoS_2 synthesized in this method is the desorption of adsorbed hydrogen atoms to form molecular hydrogen, and that nanocrystalline MoS_2 with copiously exposed S edges are more active for HER. Photoelectrochemical measurements demonstrate the highest activity for 3-layered (<40 nm thick) MoS_2/Cu_2O photocathode fabricated at 450°C with a photocurrent of ~ 6.5 mA cm^{-2} at −0.2 V *vs*. RHE. Additionally, the MoS_2 coating helps minimize the dark current of the Cu_2O photocathode.

Introduction

The rising concerns over the increasing global energy demand and negative impact on the environment of fossil fuels have stimulated great efforts towards developing clean and renewable energy alternatives.[1-3] Abundantly available, solar energy holds the promise of addressing this global energy challenge. To date, various emerging strategies and scale-up approaches are employed toward commercialization of various electrodes and catalysts for solar fuel device applications.[4-8] Direct solar energy-driven photoelectrochemical (PEC) water splitting by employing semiconductor photocatalysts offer a direct and sustainable way to generate hydrogen.[9-11] Semiconductor-based PEC water splitting involves 1) light absorption by the semiconductor electrode, 2) charge separation at the semiconductor-electrolyte interface, 3) charge transport in the semiconductor, and 4) interfacial charge transfer to produce H_2 and O_2 at cathode and anode, respectively.[12] Each of the four steps plays critical roles in governing the overall operation efficiency of a PEC system. Cuprous oxide (Cu_2O) is among the attractive *p*-type semiconducting materials with a suitable band gap for sunlight absorption and 18% theoretical PEC water splitting efficiency.[13] Cu_2O is also easy to synthesize with tunable morphologies having multi-faceted structures.[14-16] Because the valence band of Cu_2O originates mainly from the more diffuse and less directional Cu *d* orbitals than O *p* orbitals, the effective mass of the hole is lower. As a result, Cu_2O possesses excellent electrical properties such as a long carrier diffusion length[17] up to several micrometers and high hole mobility[18] of 100 cm^2 V^{-1} s^{-1}, leading to efficient charge transport and separation in an electrochemical device. Cu_2O has been widely

[a] Department of Chemistry, The University of Alabama, Tuscaloosa, Alabama 35487, USA.
[b] Center for Materials for Information Technology, The University of Alabama, Tuscaloosa, Alabama 35487, USA.
[c] Department of Chemistry, Tulane University, New Orleans, Louisiana 70118, USA.
[d] Department of Chemical and Biological Engineering, The University of Alabama, Tuscaloosa, Alabama 35487, USA.
[e] Department of Chemistry and Biochemistry, University of Mississippi, Oxford, Mississippi 38655, USA.
[f] Department of Electrical and Computer Engineering, The University of Alabama, Tuscaloosa, Alabama 35487, USA.

†Electronic Supplementary Information (ESI) available: Polarization curves of MoS_2 at different rpms; Koutecky–Levich plots, CV of ferrocene, CVs of MoS_2 precursors in DMF, Polarization curves of MoS_2/FTO, CVs of bare FTO, as-grown and N_2-annealed MoS_2 at different scan rates, CVs by Pt electrode for ORR activity from N_2-saturated, freshly-prepared and O_2-saturated Na_2SO_4 electrolytes at different scan rates, EDS of Cu_2O and MoS_2/Cu_2O, EDS mapping of cross-sectional MoS_2/Cu_2O, SEM of N_2-annealed Cu_2O and MoS_2, Photocurrents of N_2-annealed MoS_2-modified Cu_2O with varying MoS_2 layers, XRD and SEM of N_2-annealed Cu_2O before and after PEC, Photocurrents of as-grown MoS_2-modified Cu_2O, IPCE under backside illumination, Long-term photostability tests of as-grown Cu_2O and N_2-annealed MoS_2-modified Cu_2O, XRD patterns and SEM images of as-grown Cu_2O and N_2-annealed MoS_2-modified Cu_2O before and after 1 h stability test. See DOI: 10.1039/x0xx00000x

exploited as a hole transport layer in planar *p-i-n* junction perovskite solar cells leading to high conversion efficiencies.[19] Additional merits

Table 1 Recent literature on protected Cu_2O photocathode for solar water splitting

#	Cu_2O	Protective layer(s)	PEC Performance	Reference
1	Electrodeposition (lactate bath) 1.3 μm thick	5 nm Al:ZnO+11 nm TiO_2 by ALD and Pt NPs by electrodeposition (ED) (on FTO)	J_{ph}=−7.60 mA cm^{-2} @0 V_{RHE} from 1.0 M Na_2SO_4 buffered at pH 4.9 with 0.1 M KPi.	*Nat. Mater.*[13]
2	Electrodeposition (lactate bath) 200 nm thick	20 nm Al:ZnO+100 nm TiO_2 by ALD, 40 nm RuO_x by photodeposition on Au, NiO, and NiO/CuO-coated FTO substrates	J_{ph}=−5.20 mA cm^{-2} @0 V_{RHE} from 0.5 M Na_2SO_4 and 0.1 M KPi at pH 5.0.	*Energy Environ. Sci*[20]
3	Electrodeposition (lactate bath) 500 nm thick	20 nm Al:ZnO+100 nm TiO_2 by ALD, 40 nm RuO_x by photodeposition and Pt NPs by ED (on FTO)	J_{ph}=−5.00 mA cm^{-2} @0 V_{RHE} from 1.0 M Na_2SO_4 buffered at pH 5.0 with 0.1 M KPi.	*Energy Environ. Sci.*[21]
4	Electrodeposition (lactate bath) 500 nm thick	Amorphous MoS_2: 20 nm Al:ZnO +100 nm TiO_2 by ALD and 100 nm MoS_2 by CV from 0.2 mM aqueous solution of $(NH_4)_2MoS_4$ + 0.1 M $NaClO_4$ (pH 6.8) and Pt NPs by ED (on FTO)	J_{ph}=−2.70 mA cm^{-2} @0 V_{RHE} from 1.0 M Na_2SO_4 buffered at pH 5.0 with 0.1M K_3PO_4 and −5.70 mA cm^{-2} @0 V_{RHE} from H_2SO_4 at pH 1.0	*Nat. Commun.*[22]
5	Anodization, $Cu(OH)_2$/Cu to Cu_2O NWs	20 nm Ga_2O_3+15 nm TiO_2 by ALD (annealed at 220°C) and Pt NPs by ED	J_{ph}=−2.95 mA cm^{-2} @0 V_{RHE} from 0.5 M Na_2SO_4-0.1 M KH_2PO_4 buffered at pH 4.3.	*Energy Environ. Sci.*[23]
6	Anodization $Cu(OH)_2$	Graphene: $Cu(OH)_2$ NWA/Cu mesh in aqueous GO dispersion solution (20 min), dried, annealed at 500°C in an N_2 for 4 h (on Cu mesh)	J_{ph}=−4.80 mA cm^{-2} @0 V_{RHE} from 1.0 M Na_2SO_4 buffered at pH 5.0 with 0.1 M KPi.	*J. Mater. Chem. A*[24]
7	Electrodeposition (lactate bath) 2.3 μm thick	2.7 μm thick porous Cu_2MoS_4 by drop-casting and 32 nm NiO by spin-coating 0.5 M $Ni(OAc)_2$ in 2-methoxyethanol, air-annealing at 220°C for 30 min (on FTO)	J_{ph}=−1.25 mA cm^{-2} @0 V_{RHE} from 1.0 M Na_2SO_4 buffered at pH 5.0 with $NaHSO_4$.	*Nanoscale*[25]
8	Electrodeposition (lactate bath) 1.3 μm thick	NiFe-LDH from 0.2 M [$Ni(NO_3)_2 \cdot 6H_2O$] and 0.1 M [$Fe(NO_3)_3 \cdot 9H_2O$] at −1.0 V *vs*. Ag/AgCl for few 20 s (on FTO)	J_{ph}=~−2.50 mA cm^{-2} @0 V_{RHE} (At −0.6$V_{Ag/AgCl}$) from 0.5 M Na_2SO_4 at pH 6.8 without buffer.	*Sci. Rep.*[26]

such as low-cost and proper straddling of its energy bands for the water reduction and oxidation potential levels make Cu_2O an attractive photocathode to achieve visible-light-driven proton reduction for producing H_2 from water. Unfortunately, the use of Cu_2O as a photocathode for water reduction is hindered by its poor stability in aqueous solution. Both redox potentials for reducing Cu_2O to Cu and oxidizing Cu_2O to CuO lie within the bandgap of Cu_2O, limiting its durability for PEC energy conversion. Several methodologies have been developed to address the stability issue of Cu_2O (Table 1). For example, ultrathin Al:ZnO interlayer and a few nm TiO_2 coated with RuO_x or MoS_2 and Pt nanoparticles (NPs) have been used to modify the surface of electrodeposited Cu_2O to reduce its decomposition during water reduction reaction and enhance the photocurrent up to 7 mA cm^{-2} at 0 V versus reversible hydrogen electrode (RHE).[13, 21, 22] ALD coating of Ga_2O_3 thin film buffer layer resulted in a stable performance from TiO_2-coated Cu_2O-based photocathodes with higher photovoltage and positive onset potential.[23] Pt NPs are used as co-catalysts in these studies for hydrogen evolution reaction (HER), although large-scale applications of expensive precious metals in such PEC solar fuel system are severely limited. Pt-free materials such as graphene oxide, porous Cu_2MoS_4 followed by NiO layer and NiFe layered double hydroxide (LDH) structures have been developed to partially address the stability issue of Cu_2O.[24-26] Recently, Grätzel group reported a photocurrent density of 5.2 mA cm^{-2} at 0 V *vs*. RHE using a slightly modified Pt-free approach that makes use of a hole-selective under layer of NiO/CuO on FTO substrate.[20] Transition metal dichalcogenides (TMDs), such as molybdenum sulfide (MoS_2) and tungsten sulfide (WS_2), have shown good prospects as electrocatalyst for HER[27-34] and they can serve as a surface protection layer on Cu_2O to facilitate efficient charge separation from Cu_2O and rapid electron transfer to the catalytically active S sites of TMDs for enhanced HER. Recently, Sb_2Se_3[35] and WSe_2[36] have been explored as the promising binary photocathode materials for efficient solar hydrogen production. Herein, we report a simple synthesis and strategic coating approach by which MoS2 coating is achieved on electrodeposited Cu_2O using a precursor derivative of molybdenum sulfide [$Mo_3S_7(S_2CNEt_2)_3$]I that can be easily spin-coated while maintaining good adherence to the Cu_2O to

protect its surface and enhance PEC activity. Fig. 1 shows the molecular structure of $[Mo_3S_7(S_2CNEt_2)_3]I$ precursor and a schematic of solar water splitting system to generate hydrogen using MoS_2-modified Cu_2O photocathode. With the catalytically active, protective and stable MoS_2 coating achieved from such precursor, the photo-generated electrons can be

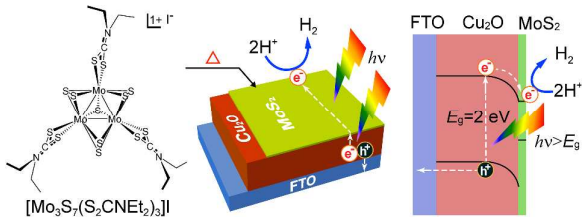

Fig. 1 Schematic of a synthesis strategy to prepare surface-passivated Cu_2O photocathode (MoS_2/Cu_2O/FTO) using MoS_2 (molecular structure of MoS_2 precursor is shown) as a bifunctional material to protect Cu_2O and perform HER catalysis for solar water splitting application.

effectively transported from the light-absorbing Cu_2O to the catalytic sites of MoS_2, which can catalyze the reduction of protons to produce hydrogen while preventing corrosion of Cu_2O. Such synthetic and coating approach for MoS_2 offer a solution for large-scale production of dual functional MoS_2/Cu_2O photocathode for overall PEC water splitting with solar energy.

Experimental

Materials

Copper sulfate anhydrous ($CuSO_4$, 98%, ACROS), lactic acid ($C_3H_6O_3$, 85.0-90.0%, Alfa Aesar), sodium hydroxide (NaOH beads, VWR), sodium sulfate anhydrous (Na_2SO_4, 99%, Fisher Scientific), acetone, absolute ethanol, and ethanol, tetrahydrofuran (THF) were used as-received without further purification. All the solutions were freshly prepared using deionized water (resistivity <18 MΩ·cm). Commercially available transparent conducting fluorine-doped tin oxide (FTO, 15-20 $\Omega\cdot cm^{-1}$, 1.5 × 1.5 cm^2) coated glass substrates were used.

Electrodeposition of Cu_2O films

Prior to electrodeposition, the FTO substrates were cleaned successively using detergent followed by acetone, ethanol and deionized water in an ultrasonic bath each for 10 min, dried using a N_2 gas stream, and finally treated by UV-ozone for 15 min. Electrodeposition of Cu_2O was carried out using a slightly modified method reported in the literature.[16] Briefly, Cu_2O was electrodeposited from a lactate-stabilized solution (pH 11.0) consisting of 0.4 M $CuSO_4$ and 3.0 M lactic acid using an electrochemical workstation CHI760C (CH Instruments, Inc., Austin, TX) at room temperature in a three-electrode configuration with FTO glass substrate as working electrode (~2 cm^2 deposition area), a graphite rod as counter electrode, and platinum coil as a quasi-reference electrode. Cu_2O was deposited at −0.3 V *vs*. Pt with a total charge of ~4.5 C for optimal film thickness (few μm).

Synthesis of MoS_2 precursor derivatives and MoS_2 coating on Cu_2O

The solvents employed for synthesis of MoS_2 precursor derivatives were dried with a system of drying columns from the Glass Contour Company (CH_2Cl_2, hexanes), purchased in an ultra-dry grade (*N*, *N*-dimethylformamide), or simply used as received from commercial sources. Tetraethylthiuram disulfide was also used as supplied from a commercial vendor. Literature procedures were used in the preparations of $[NH_4]_2[Mo_3S_{13}]$[37] and $[Mo_3S_7(S_2CNEt_2)_3]I$.[38] The related dimethyldithiocarbate derivative, $[Mo_3S_7(S_2CNMe_2)_3]I$, was also prepared by the method of Hegetschweiler and coworkers[38] but from $[Ph_4P]_2[Mo_3S_7Br_6]$ rather than $[Et_4N]_2[Mo_3S_7Br_6]$. The $[Bu_4N]^+$ salt of $[Mo_3S_{13}]^{2-}$ was prepared from $[NH_4]_2[Mo_3S_{13}]$ by base neutralization with $[Bu_4N][OH]$, as described by McDonald and coworkers.[39] The $[Mo_3S_7(S_2CNEt_2)_3]^+$ cation can be prepared either by displacement of Br^- from $[Mo_3S_7Br_6]^{2-}$ by the dithiocarbamate anion or by oxidation and displacement of terminal disulfide with the tetrathiuram disulfide (Scheme 1). This compound type crystallizes well and in reproducible fashion with the I^- counteranion, which forms particularly favorable $S_{ax}\cdots I^-$ soft-soft interactions on the underside of the cluster opposite the μ_3-sulfide ligand, Scheme 1D). The structure of the $[Mo_3S_7(S_2CNEt_2)_3]^+$ cation reveals an idealized C_{3v} symmetry in multiple independent X-ray diffraction studies with varying counteranions. (I^-,[38, 40, 41] Br^-,[42] Cl^-,[43] ClO_4^-,[40] ½S^{2-},[44] $-S_2CNEt_2$,[45] TCNQ[46] (TCNQ= tetracyanoquinodimethane)). Electrochemical characteristics of $[Mo_3S_7(S_2CNEt_2)_3]I$ are described in the Supporting Information, (Fig. S1 and S2). To achieve MoS_2 coating on Cu_2O films, first, the precursor was dissolved in an appropriate solvent and spin-coated onto Cu_2O films. The desired MoS_2 coating thickness was

Journal Name

ARTICLE

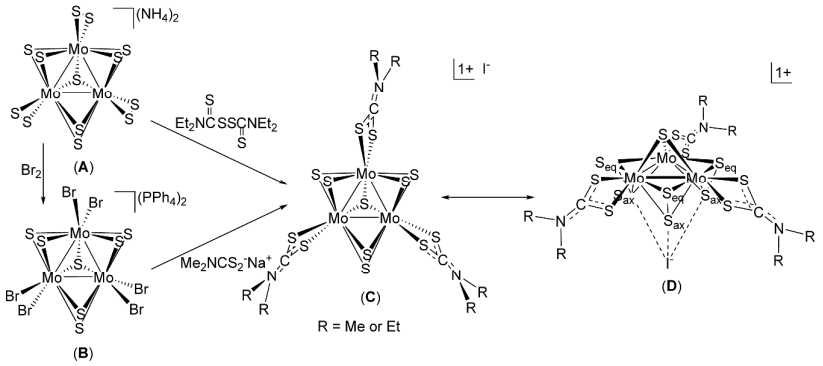

Scheme 1 Synthesis of (C) $[Mo_3S7(S_2CNEt_2)_3]I$ cluster from either (A) $[Mo_3S_{13}]^{2-}$ or (B) $[Mo_3S_7Br_6]^{2-}$. Image (D) shows an orientation of $[Mo_3S_7(S_2CNEt_2)_3]I$ with the Mo_3 plane orthogonal to the plane of the paper.

optimized by adjusting the precursor concentration as well as number of spin-coated layers.

Characterization of $[Mo_3S_7(S_2CNEt_2)_3]I$ decomposition and fabrication of MoS_2 electrodes

The thermal behavior of as-synthesized $[Mo_3S_7(S_2CNEt_2)_3]I$ The TGA/DSC measurements were performed by heating the powder in an Al_2O_3 crucible under flowing argon at a heating rate of 2 °C min^{-1} from room temperature to 600 °C. The structural analysis of as-grown Cu_2O and N_2-annealed MoS_2- a thermogravimetric analyzer (SETARAM SETSYS), which performed thermogravimetric analysis (TGA) and differential powder (a precursor for coating MoS_2 film) was examined using scanning calorimetry (DSC) simultaneously. coated Cu_2O samples was performed using a Bruker D8 Discover X-ray diffractometer equipped with Co-Kα radiation source operated at 40 kV and 30 mA. The X-ray diffraction (XRD) patterns were recorded in the 2θ range of 20-100°. The phase identification was done using Bruker GADDS software with the help of a standard diffraction database (ICDD). The surface and cross-sectional morphology, and the chemical composition of films were examined using a JEOL 700 scanning electron microscope (SEM) equipped with an X-ray energy dispersive spectrometer (EDS). High-resolution transmission electron microscopy (HRTEM) images of Cu_2O and MoS_2-modified Cu_2O were acquired from a FEI TECNAI F20 transmission electron microscope. A TESCAN LYRA focus ion beam-field emission scanning electron microscope (FIB-FESEM) was used to image the surface topography of MoS_2 on FTO. To prepare a FIB specimen for thickness measurement of 3-layered MoS_2 spin-coated on FTO, a platinum bar was deposited on top of MoS_2 through a gas injection system to lift it out using omniprobe and attach on a copper grid for the TEM measurement. The extracted wedge was thinned to a thickness of less than ~100 nm. A FEI TECNAI F20 TEM beam was accelerated at 200 kV to obtain bright field images and diffraction patterns. Raman spectra were recorded with a Horiba LabRAM HR Evolution Raman spectrometer system in the air at room temperature using a 633-nm wavelength laser. The laser was focused onto the sample using a 100X objective. An ultra-low frequency (ULF) filter and a grating with 1800 grooves/mm were used. The rotating ring disc electrode (RRDE), polarization and photocurrent measurements were performed using an electrochemical workstation (CHI 760C, CH Instruments). The RRDE voltammograms were recorded on a RRDE configuration (ALS Co., Ltd, Japan) with a glassy carbon (GC) disc and Pt ring electrode. The geometric area of Pt ring was 0.75 cm^2 (ID=0.5 cm and OD=0.7 cm). The GC disc with a geometric area of 0.50 cm^2 was used as the substrate for deposition of MoS_2 catalyst. Prior to catalyst deposition, the RRDE was initially polished with a 0.3 μm alumina (Buehler) slurry on a Nylon pad and subsequently with 0.05 μm alumina slurry on a micro-cloth (CH Instruments) and then cleaned with deionized water ultrasonically. MoS_2 electrocatalyst was prepared on GCE by drop-casting and air-drying a microliter drop of 5 mM MoS_2 precursor solution in THF. The HER activity of MoS_2 was tested in 0.5 M H_2SO_4 electrolyte using RRDE voltammograms recorded at the rotation frequencies from 0 to 5000 rpm. The potential range for HER scans is chosen such that excessive H_2 bubbling is avoided. All electrochemical, as well as PEC measurements, were carried out at room temperatures in a three-electrode system consisting of photocathode as the working electrode, a saturated calomel electrode (SCE, *sat*. KCl) or silver/silver chloride (Ag/AgCl, *sat*. KCl) as reference electrode, and a counter electrode such as

platinum. Unless otherwise specified, all potentials in this work are measured against the SCE or Ag/AgCl reference electrodes and are reported versus reversible hydrogen electrode (RHE) using Nernst equation (1):[47],

$$E_{\mathrm{RHE}} = E_{\mathrm{Reference}} + 0.059\ \mathrm{pH} + E^{\mathrm{o}}_{\mathrm{Reference}} \quad (1)$$

where E_{RHE} is the converted potential *vs*. RHE, $E_{\mathrm{Reference}}$ is the experimental potential measured against the reference electrode (SCE or Ag/AgCl), and $E^{\mathrm{o}}_{\mathrm{Reference}}$ is the standard potential of refthe erence electrode (0.242 V for SCE and 0.1976 V for Ag/AgCl at 25 °C). Cyclic voltammograms (CVs) were recorded for proton reduction studies using MoS_2-coated glassy carbon or FTO electrodes in 0.5 M H_2SO_4 electrolyte at the scan rate of 50 mV s^{-1}. All CVs were all corrected for the *iR* contribution using CHI instrument. The photoelectrochemical measurements of as-grown and MoS_2-modified Cu_2O photocathodes were performed in 0.5 M Na_2SO_4 electrolyte (pH 6.7). Alternatively, CVs were recorded for FTO, as-grown and N_2-annealed MoS_2/FTO, and Pt disc electrode (2 mm diameter) to investigate the proton reduction and/or oxygen reduction reaction (ORR). Unless otherwise mentioned, all the PEC or electrochemical (ORR/HER) measurements using MoS_2, MoS_2-modified Cu_2O or Pt electrodes were performed in aerobic (freshly-prepared or O_2-saturated) and anaerobic (N_2-saturated) near-neutral 0.5 M Na_2SO_4 electrolytes at room temperature. High-purity N_2 or O_2 gases were rigorously purged into the electrolyte for at least one hour at the rate of 30 mL min^{-1}. The electrolyte was deaerated with high-purity N_2 to eliminate the effect of oxygen reduction. Although MoS_2 is known as HER catalyst like Pt, we also explored its ability as cata alyst for oxygen reduction reaction (ORR) since 2-dimensional (2D) MoS_2[48] has recently shown such ORR activity when combined with carbon-based electrodes.[49] A standard simulated 1 sun (intensity of 100 mW cm^{-2}) irradiation was provided with the help of a solar simulator using a 300 W xenon lamp (Oriel AM 1.5 filtered, Newport) light source. The *J-V* curves of photocathodes were recorded using linear sweep voltammetry (LSV) at a scan rate of 50 mV s^{-1} under chopped light at a frequency of 2.5 Hz with front-side illumination. Incident photon to light conversion efficiency (IPCE) or action spectra were measured using the same xenon lamp and a monochromator in the wavelength range of 400-700 nm. The photocathode was fixed inside a three-arm PEC cell and illuminated from the substrate side (backside) as well as the film side (frontside). The photocurrent responses at each wavelength were collected by measuring chronoamperometric *J-t* curves in a three-electrode configuration at ~0.2 V *vs*. RHE in 0.5 M Na_2SO_4. The power density of the monochromatic light was measured using a calibrated silicon photodiode (THORLABS, S110C) to determine the IPCE values at each wavelength. Electrochemical impedance spectroscopy (EIS) and Mott-Schottky (MS) studies were performed using the same electrochemical workstation (CHI 760C), which is equipped with an electrochemical interface and impedance analyser facility. The EIS curves were recorded from 100 kHz to 0.1 Hz at the water reduction potential of 0.0 V *vs*. RHE (−0.6 V *vs*. Ag/AgCl) under 1 sun illumination. A ZView program (Scribner Associates Inc.) was used to fit the EIS data with a suitable equivalent circuit model. The MS measurements were performed in the dark by sweeping a DC potential from −0.5 to 0.2 V *vs*. Ag/AgCl at an AC frequency of 1 kHz. The amplitude of AC signal was 10 mV for both EIS and MS measurements. Optical absorption of the films was studied (wavelength range: 400-700 nm) using a UV-vis spectrophotometer (Perkin Elmer Lambda 35).

Results and Discussion

To quickly gain insight into the HER electrocatalytic activity of MoS2 derived from $[Mo_3S_7(S_2CNEt_2)_3]I$ precursor, rotating ring-disc electrode (RRDE) voltammograms were carried out based on a RRDE configuration with a glassy carbon disc electrode (GCE) and Pt ring electrode. Fig. 2A shows the polarization curves for HER of GCE and MoS_2-modified GCE recorded at 5000 rpm in 0.5 M H_2SO_4 electrolyte. The protons are reduced on the glassy carbon disc (with or without MoS_x coating) resulting in HER current and are then oxidized at the Pt ring, as shown schematically in the inset of Fig. 2A, to produce oxidation current. Pt ring electrode potential was held constant at 0.4 V *vs*. SCE (0.65 V *vs*. RHE), which is sufficiently positive to oxidize hydrogen from the GC disc electrode. Both disc and ring current densities of MoS_2-modified GCE are remarkably higher than those of GCE. For better HER or ORR activity, the catalyst should have a lower overpotential, which is basically the difference between the applied potential and the

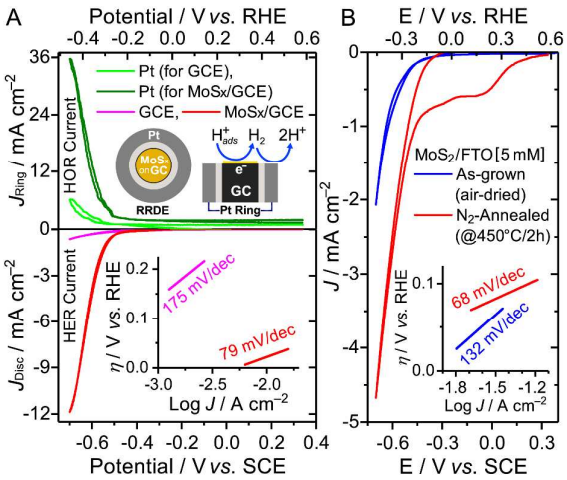

Fig. 2 (A) RRDE response (rotation speed 5000 rpm) for bare GCE and 5.0 mM MoS_2/GCE; Inset shows the Tafel slope for each electrode. (B) Polarization curves of as-grown and N_2-annealed MoS_2/FTO electrodes for proton reduction. Scan rate: 50 mV s^{-1}; Electrolyte: 0.5 M H_2SO_4.

thermodynamic potentials of a given electrochemical reaction. The polarization curves are replotted as overpotential (η) against the logarithm of current density (log *J*) in the inset of Fig. 2A to obtain Tafel plots for assessing the HER kinetics of MoS_2- modified GC electrode. The Tafel slope is an intrinsic property of an electrocatalyst and can be used to probe the elementary steps involved in H_2 evolution, providing insights into the HER mechanism. The linear portion of the Tafel plots

are fit to the Tafel equation ($\eta = b \log J/J_0$, where J is the current density, J_0 is the exchange current density, and b is the Tafel slope), yielding Tafel slopes of about 79 and 175 mV dec^{-1} for MoS_2/GCE and bare GCE, respectively. The lower Tafel slope of 79 mV dec^{-1} and higher exchange current density of 1.31 mA cm^{-2} for MoS_2/GCE as compared to bare GCE (b=175 mV dec^{-1} and J_0=0.04 mA cm^{-2}) strongly suggest that MoS_2 prepared from $[Mo_3S_7(S_2CNEt_2)_3]I$ is a promising HER catalyst. The onset potential for HER activity for such MoS_x is around -0.2 V vs. RHE, which is better than the MoS_2 nanosheets and close to the state of the art Pt/C catalyst tested using RRDE (~0 V vs. RHE).[50] Generally, Gibb's free energy change (ΔG_H) is regarded as a reasonable descriptor of HER activity for a wide variety of catalysts and it is suggested to have optimum HER activity at $\Delta G_H \approx 0$. The lower ΔG_H can lead to very high surface coverage of H_{ads}, while higher ΔG_H will cause the protons to be bonded too weakly on the catalyst surface, which both lead to sluggish HER kinetics. Both density functional theory (DFT)[32] calculations and experimental[51] studies have shown that the MoS_2 edge sites with unsaturated sulfur atoms can lower the ΔG_H approaching 0. The MoS_2 reduces the protons at low overpotential via coordinated sulfur edge sites ($(10\bar{1}0)$ planes on edges of MoS_2), while its basal (0001) planes are catalytically inactive.[51] Thus, nanocrystalline MoS_2 with copiously exposed S edges is more active for HER than its inert bulk forms. This understanding has led to significant efforts for developing nanostructured MoS_2-based HER catalysts to maximize the number of edge sites, including amorphous, crystalline, and hybrid materials.[52] The HER activity in acidic media is proposed to follow two separate pathways (the Volmer–Tafel or the Volmer–Heyrovsky mechanism) for reducing protons (H^+) to hydrogen (H_2)[52, 53], which proceeds through three possible reaction steps.[53, 54] Depending on different Tafel slopes, the rate-limiting steps can be electrochemical hydrogen adsorption, $H_3O^+ + e^- \rightarrow H_{ads} + H_2O$ (Tafel slope of 120 mV dec^{-1}), electrochemical desorption, $H_{ads} + H_3O^+ + e^- \rightarrow H_2 + H_2O$ (Tafel slope of 40-120 mV dec^{-1}), and chemical desorption, $H_{ads} + H_{ads} \rightarrow H_2$ (Tafel slope of 30-40 mV dec^{-1}).[52, 53] The rate-limiting step of HER on our MoS_2 catalyst is electrochemical desorption because of its low Tafel slope. The polarization curves data for MoS_2 on GCE obtained at −0.36 V *vs*. RHE for different rotation speeds yielded a linear Koutecky–Levich plot over the entire rotation frequency range tested at both disc and ring electrodes (Fig. S3). The slope of Koutecky–Levich plot for MoS_2 on disc electrode is close to one (n=0.95), which suggests that the electrochemical adsorption of hydrogen proceeds at potentials near the onset by consuming one electron and then combining with another adsorbed hydrogen to evolve hydrogen gas at more cathodic potentials. To further

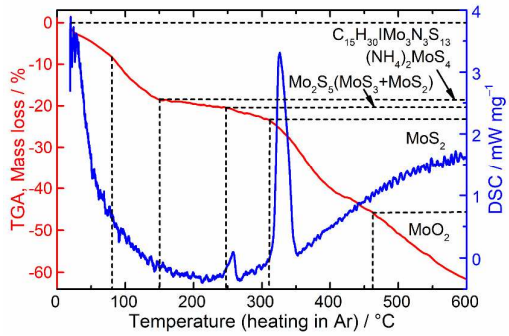

Fig. 3 TGA/DSC profiles of MoS_2 precursor ($[Mo_3S_7(S_2CNMe_2)_3]I$) in Ar atmosphere.

assess the electrocatalytic proton reduction HER activity of MoS_2 upon annealing treatment on transparent conducting substrates, a 5-mM solution of MoS_2 in THF was spin-coated onto the FTO substrates. Electrocatalytic activity for proton reduction by MoS_2 catalyst, before and after annealing at 450 °C in N_2 atmosphere, was investigated by cyclic voltammetry (CV) in 0.5 M H_2SO_4 electrolyte. In Fig. 2B, the lower Tafel slope of 68 mV dec^{-1} with exchange current density of 1.95 mA cm^{-2}) for N_2-annealed MoS_2 as compared to air-dried MoS_2 (b=132 mV dec^{-1} and J_0=10.28 mA cm^{-2}) indicates that spin-coated MoS_2 supports kinetically favorable HER than bare GC electrode. In other words, N_2-annealed MoS_2 drives a large catalytic current density of 10 mA cm^{-2} at a low overpotential of 0.002 V compared to the as-grown MoS_2, which requires at least 0.048 V for HER.

The simultaneous TGA/DSC analysis of $[Mo_3S_7(S_2CNEt_2)_3]I$ in Ar environment was performed to observe the thermolysis of $[Mo_3S_7(S_2CNEt_2)_3]I$ and the subsequent crystallization behavior of MoS_2. Fig. 3 shows the TGA/DSC profiles of $[Mo_3S_7(S_2CNEt_2)_3]I$ under flowing Ar gas. The profiles suggest a series of reactions with continuous weight losses upon heating from room temperature to 600 °C. Five decomposition steps can be identified from the TGA curve with mass loss ratios of 8.2, 18.3, 20.5, 23.3 and 45.8%, respectively. The first decomposition at around 80 °C arises from the dehydration of the starting precursor material, which results in 8.2% mass loss. The second

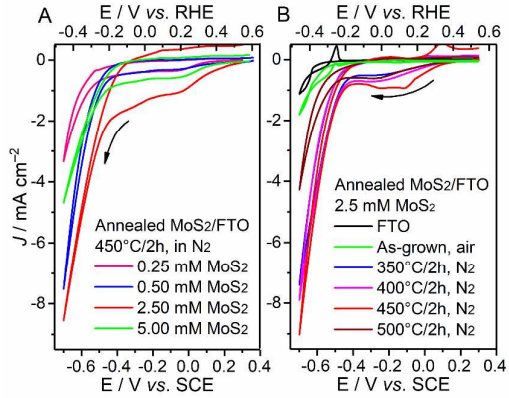

Fig. 4 Effect of MoS_2 film thickness (A) and N_2-annealing temperature (B) on proton reduction current density of MoS_2/FTO electrodes

in the range of 80-150 °C, causing an accumulated mass loss of 26.5% (8.2%+18.3%), is attributed to the formation of $(NH_4)_2MoS_4$. For the third decomposition, a mixture of MoS_3/MoS_2 (in a ratio of 1:1) is likely formed in the temperature range of 150–245 °C leading to a total weight loss of 20.5%, which implies a transition from $(NH_4)_2MoS_4$ to MoS_2. In the temperature range of 245-310 °C, the MoS_2 is formed at a mass loss of 23.3%. In the temperature range of 310-462 °C, the crystalline transformation of MoS_2 occurs. However, with a mass loss of 45.8%, MoS_2 is converted into MoO_2 at higher temperatures, possibly due to residual oxygen present in the crucible. The presence of two distinct exothermic peaks at 258 and 325 °C also confirms the phase transformations from amorphous mixed (MoS_3+MoS_2) to the crystalline MoS_2 material. Hence, the annealing temperature window of 350-450 °C is best suited to produce the crystalline MoS_2 phase.

Fig. 4A shows proton reduction HER characteristics of MoS_2/FTO electrodes fabricated at 450 °C by spin-coating different concentrations of $[Mo_3S_7(S_2CNEt_2)_3]I$ precursor in THF. The precursor concentration was varied from 0.25 to 5.0 mM. MoS_2 film coated from 2.5 mM precursor derivative gives optimal proton reduction performance. Additionally, to determine the appropriate temperature to fabricate active MoS_2 coating, the N_2-annealing temperature was varied from 350 to 500 °C at intervals of 50 °C by keeping a fixed precursor concentration of 2.5 mM (See Fig. 4B). The annealing study suggests that a MoS_2/FTO electrode fabricated at 450 °C gives optimum HER performance. Such electrode exhibits a Tafel slope of −40 mV dec^{-1} (not shown) and exchange current density of 0.33 mA cm^{-2}, which suggests that N_2-annealed MoS_2 can drive a large catalytic current density (for instance, 10 mA cm^{-2}) for a small overpotential of 0.06 V *vs*. RHE. According to HER kinetic models, a Tafel slope of 40 mV dec^{-1} (< 120 mV dec^{-1}) for N_2-annealed MoS_2 in 0.5 M H_2SO_4 is closer to the lowest value measured till now for MoS_2-based HER catalysts, even approaching that of ~30 mV dec^{-1} for Pt/C catalysts[52] and follows a Volmer-Tafel rate-determining step mechanism.[53] Thus, N_2-annealed MoS_2 exhibits relatively higher electrocatalytic performance as an efficient HER catalyst with lower onset potential, high catalytic exchange current density, and a small Tafel slope. This enhancement can be ascribed to the formation of crystalline MoS_2 with adequate exposure of catalytically active sites. The $[Mo_3S_7(S_2CNMe_2)_3]I$ and other derivatives of MoS_2 such as $Mo_3S_7(S_2CNEt_2)_3I$, $Mo_3S_4(S_2CNEt_2)_4$, $(NH_4)_2[Mo_3S_{13}]$, and $(Bu_4N_2)[Mo_3S_{13}]$ were also investigated for the proton reduction. These precursors were dissolved in different solvents such as THF, DMF, or CH_2Cl_2, spin-coated onto conducting FTO glass substrates, and N_2-annealed at 450 °C for 1 h. Owing to their limited solubility, precursor concentrations of 1.0 mM were employed for all derivatives such that, for purposes of comparison, all MoS_2 films were prepared under a common set of conditions. The proton reduction HER curves for all the derivatives are shown in Fig. S4. Among them, $[Mo_3S_7(S_2CNMe_2)_3]I$ prepared from THF exhibited the most promising HER activity. Thus, $[Mo_3S_7(S_2CNMe_2)_3]I$ was chosen for our further studies with Cu_2O photocathodes. The catalytic activities of MoS_2 electrodes prepared with optimal synthesis conditions (2.5 mM precursor concentration and 450°C annealing temperature in N_2) and their counterparts are investigated in a near-neutral 0.5 M Na_2SO_4 electrolyte and compared with a platinum disc electrode. Fig. S5 shows the corresponding CVs of bare FTO, as-grown MoS_2 (air-dried for 1 min and 15 h), and N_2-annealed MoS_2 electrodes recorded at the scan rate of 50 mV s^{-1} from freshly prepared and 2 h-degassed (O_2-free) 0.5 M Na_2SO_4 electrolytes. N_2-annealed MoS_2/FTO sample shows better catalytic activity towards proton reduction in N_2-saturated Na_2SO_4 electrolyte than the as-synthesized MoS_2/FTO sample. CVs at different scan rates for all the samples in oxygen-free and oxygenated Na_2SO_4 electrolyte also show a similar trend (Fig. S6). The ORR and HER activities in oxygen-free and oxygenated near-neutral 0.5 M Na_2SO_4 are studied using a standard Pt disc electrode at different scan rates (Fig. S7). As seen from the overlay of CVs at the scan rate of 50 mV s^{-1} (Fig. S7D), no oxygen reduction peak is seen for oxygenated Na_2SO_4 electrolyte although the cathodic current density is relatively higher than the background current (O_2-free N_2-saturated electrolyte). On the other hand, the proton reduction current density is higher for N_2-saturated electrolytes at more electronegative potentials.

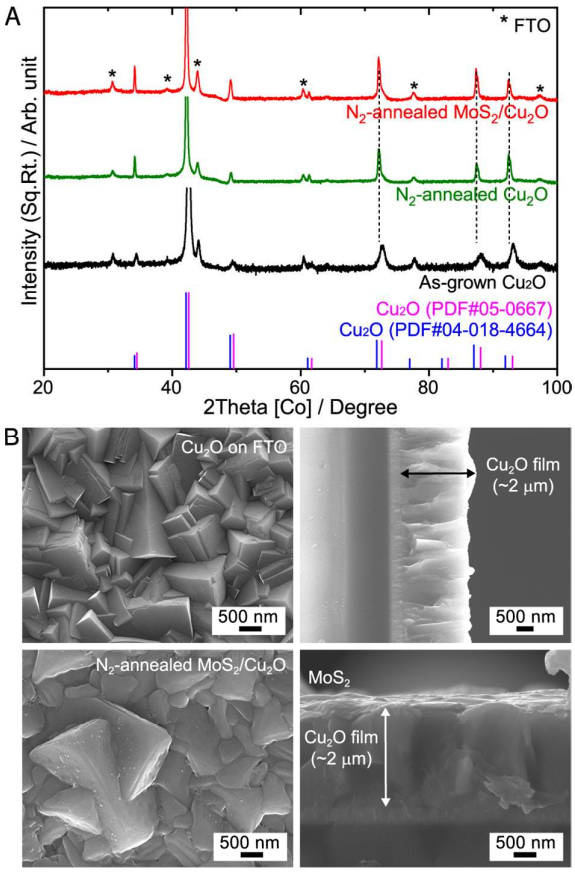

Fig. 5 (A) Normalized XRD patterns of as-grown Cu_2O/FTO, N_2-annealed Cu_2O/FTO, and N_2-annealed MoS_2/Cu_2O/FTO electrodes. (B) Surface and cross-sectional SEM images of as-grown Cu_2O/FTO and N_2-annealed MoS_2/Cu_2O/FTO electrodes.

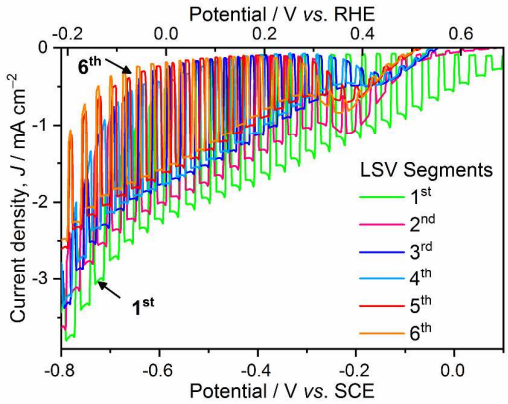

Fig. 6 Photocurrent responses of as-grown Cu_2O in 0.5 M Na_2SO_4 under 1 sun illumination and the reductive photodecomposition of Cu_2O upon repetitive LSV runs.

To study the HER characteristics of MoS_2 film on a different substrate than FTO, we studied the effect of MoS_2 coating on the PEC activities of a Cu_2O. And the electrodes were characterized by XRD and SEM prior to PEC measurement. Fig. 5A shows the normalized XRD patterns of as-grown Cu_2O, N_2-annealed Cu_2O, and N_2-annealed MoS_2-modified Cu_2O films. All the synthesized films are polycrystalline. As-grown Cu_2O are indexed to the cubic Cu_2O phase with a lattice constant of a=4.2696 Å. The diffraction peaks of as-grown Cu_2O at 34.45°, 42.56°, 49.39°, 72.54°, 88° and 93.14° correspond to the diffraction from (110), (111), (200), (220), (311) and (222) planes of Cu_2O (ICDD PDF#05-0667). No discernible peaks of CuO or Cu are seen. The peaks marked by asterisks are due to the FTO substrate. All the samples exhibit a dominant peak at ~42° indicating highly oriented (111) Cu_2O plane. N_2-annealed Cu_2O and MoS_2-modified Cu_2O samples show identical XRD patterns with enhanced crystallinity. N_2-annealed MoS_2/Cu_2O showed no peaks from the thin layer of MoS_2. Additionally, shift in diffraction peaks towards lower 2θ angles suggests an increase in lattice parameters, indicative of the expansion of crystal lattice. XRD patterns of annealed samples show sharp and narrow diffraction peaks with an increase in lattice parameter to 4.3108 Å. Annealing causes grain growth and coalesces of grain boundaries resulting in the ordered crystal structure. N_2-annealed MoS_2/Cu_2O shows greater crystallinity as compared to N_2-annealed Cu_2O. A larger shift in 2θ angle at higher angles is an indication of a reduction in the strain of the film. Both the N_2-annealed samples show no peaks of Cu or CuO. Fig. 5B shows the representative SEM images of as-grown Cu_2O and N_2-annealed MoS_2/Cu_2O films prepared on FTO. As-grown Cu_2O film (~ 2 μm thick) consists of polyhedral cuboidal-shaped grains with sharp edges ranging from 1 to 2 μm. The SEM image of N_2-annealed MoS_2/Cu_2O film reveals coalescence of grain boundaries. The sharp-edges of cuboidal-shaped Cu_2O grains are covered with a thin film of MoS_2. The cross-sectional SEM view shows the coverage of thin layer of MoS_2 on ~2 μm thick Cu_2O. The presence of MoS_2 was confirmed from the EDS analysis (Fig. S8). The selective cross-sectional area of MoS_2/Cu_2O along with EDS mapping (Fig. S9) reveals a film

Journal Name

ARTICLE

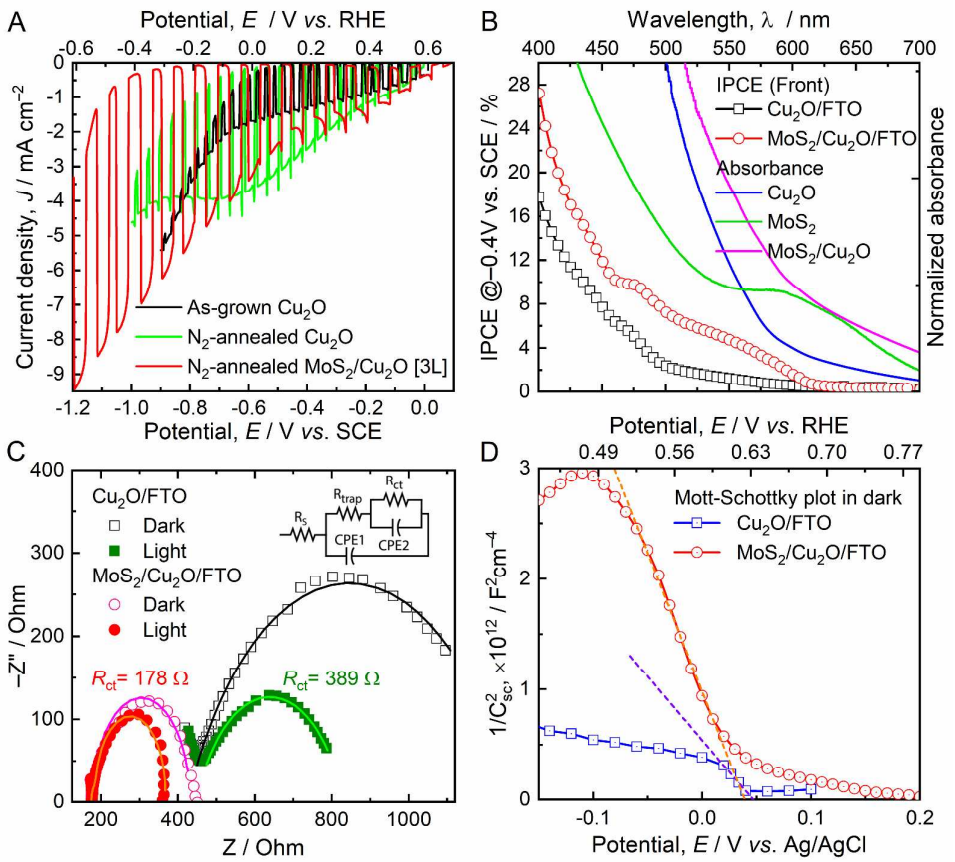

Fig. 7 (A) Photocurrent responses of as-grown Cu_2O, N_2-annealed Cu_2O, and N_2-annealed 3-layered MoS_2-modified Cu_2O photocathodes. The spin-coating layers of 2.5 mM MoS_2 precursor are varied from layer 1 (1L) to layers 4 (4L). (B) IPCE spectra of the Cu_2O and MoS_2/Cu_2O photocathodes at ~0.2 V *vs*. RHE (−0.4 V *vs*. SCE) under frontside illumination. The figure also shows the normalized absorbance of as-grown Cu_2O, MoS_2, and MoS_2-modified Cu_2O films. (C) Nyquist plots of the as-grown Cu_2O and MoS_2/Cu_2O electrodes recorded at a fixed applied potential of −0.6 V *vs*. Ag/AgCl both in dark and under the light, respectively. The inset shows the equivalent electrochemical circuit to fit the plots. The symbols and the solid lines represent the experimental and fitted data, respectively. (D) Mott-Schottky plots of as-grown Cu_2O and MoS_2/Cu_2O electrodes measured at 1 kHz frequency in dark. Electrolyte: 0.5 M Na_2SO_4 solution (pH ~6.7); light source: simulated 1 sun (100 mW cm^{-2}).

thickness of ~ 40 nm and the presence of all the constituent elements. Assuming a film thickness of 40 nm, the surface coverage of MoS_2 on Cu_2O is estimated to be 7.6158 ± 0.6 × 10^{16} molecules cm^{-2} (See Supplementary Information for details). N_2-annealed 3-layered MoS_2 is alternatively prepared on FTO, which shows continuous coverage of MoS_2 film on SnO_2 crystals (Fig. S10A) The surface morphology of N_2-annealed Cu_2O clearly shows the crystal growth (Fig. S10B). A growth of triangular-shaped crystal facets on top of the irregularly shaped crystals can be seen with few multi-faceted white overgrowths.

Fig. 6 shows the linear sweep voltammograms of as-grown Cu_2O under standard chopped light illumination measured in 0.5 M Na_2SO_4 for successive six segments. The 1st segment has negligible dark current with the onset of photocurrent toward more positive potential. The onset of dark current is at −0.6 V *vs*. SCE, which reflects the corrosion reaction. Under light illumination, photo-excited electrons of Cu_2O semiconductor travel to the conduction band of Cu_2O and reduce protons at the solid-liquid interface to form H_2 gas, while holes travel to counter electrode to oxidize water molecule to produce O_2. Photocurrent density depends on how effectively the photo-generated electron-hole pairs are separated for the two half-reactions of water splitting without any losses. The photocurrent density measured at 0 V *vs*. RHE (- 0.59 V *vs*. SCE) is 2.4 mA cm^{-2}, which is in line with the reported literature.[13]

However, recurring reduction peaks appear at ~0.4 V *vs*. RHE (−0.15/−0.20 V *vs*. SCE) during *J-V* measurements from 2nd segment onwards, which is an indication of photo-corrosion because Cu_2O undergoes reductive decomposition to Cu upon repetitive photocurrent measurements. Such change in the chemical state of the Cu_2O film after PEC measurement is observed visually by a color change from reddish brown to black and by a decrease in PEC current density. This phenomenon has been previously confirmed by SEM and XPS techniques.[13] Thus, the Cu_2O layer requires corrosion-protection to avoid direct contact between Cu_2O and the electrolyte. To suppress the photo-corrosion reaction, we passivated the Cu_2O surface with a MoS_2 layer to prevent contact with the electrolyte by using a simple approach of spin-coating and thermal annealing treatment. Fig. 7A shows the photocurrent responses of as-grown Cu_2O, N_2-annealed Cu_2O, and N_2-annealed MoS_2-modified Cu_2O (with three spin-coated layers of MoS_2) photocathodes. The photocurrent responses for other layers are shown in Fig. S11A. The photocurrent of Cu_2O increases significantly with MoS_2 modification. Photocurrent densities of 4.0 mA cm^{-2} at 0 V *vs*. RHE and as high as 6.5 mA cm^{-2} at −0.2 V *vs*. RHE are obtained for 3-layered MoS_2-modified Cu_2O photocathode. The contribution to the photocurrent due to light absorption by the MoS_2-protective overlayer is negligible. Additionally, the dark current characteristics of the Cu_2O photocathodes are improved considerably by extending the dark current onset toward anodic region by 350 mV. The reduction peak observed for as-grown Cu_2O at 0.4 V *vs.* RHE (Fig. 6) disappears after being coated with MoS_2, indicating that the Cu_2O surface is protected by the MoS_2 layer. The onset of dark current appears at −0.32 V *vs*. RHE (−0.95 V *vs*. SCE) that is well below the water reduction potential (0 V *vs*. RHE) to limit the photo-corrosion of Cu_2O. The enhanced performance of MoS_2-modified Cu_2O is attributed to uniform coverage of high concentrations of exposed edge-plane structures of MoS_2 on Cu_2O crystals, which facilitates rapid electron transport leading to significantly elevated catalytic activity. With increasing number of MoS_2 layers, the darkening of the film caused by photo-corrosion is reduced. With increasing MoS_2 thickness beyond 3 layers, however, the photocurrent decreases, which is likely because of blocking of the light by the MoS_2 film and consequent decrease of absorption by the Cu_2O electrode. The N_2-annealed Cu_2O also shows similar photocurrent response at 0 V vs. RHE as that of N_2-annealed MoS_2/Cu_2O. However, its dark current onset is only slightly better than as-grown Cu_2O. Moreover, its dark current increases after 2nd and 3rd measurements, eventually decreasing the net photocurrent response (Fig. S11B). The XRD pattern of the N_2-annealed Cu_2O sample after the PEC measurements shows the emergence of prominent metallic Cu peaks mainly at 50.55 59.11, and 88.46°, indicating a photo-induced reduction of Cu_2O to Cu that results in loss of photoactive Cu_2O material (Fig. S12A). Thus, a decrease in PEC response is due to the photocorrosion of Cu_2O, which can also be governed by the morphological changes after the PEC measurement (Fig. S12B). The triangular faceted crystals of N_2-annealed Cu_2O are broken down into nanoparticles with porous grain boundaries. Such poor photocurrent response from N2-annealed Cu_2O could be due to the certain faceted growth of Cu_2O which is prone to photocorrosion as studied previously.[14, 15] We also investigated the proton reduction performance using 3-layered as-synthesized MoS_x on Cu_2O in 0.5 M Na_2SO_4 electrolyte with and without 0.1 M K_2HPO_4 (Fig. S13). The dramatically higher photocurrent response for MoS_x-modified Cu_2O as compared to Cu_2O as well as N_2-annealed MoS_2 is encouraging. However, the as-synthesized MoS_x coating is not adherent and cannot produce similar performance upon repeated measurements. Therefore, the studies using as-synthesized MoS_x are not carried out further. IPCE is employed as a valuable diagnostic figure of merit for most PEC devices. IPCE values were calculated using relation (2),

$$\text{IPCE (\%)} = [(1240/\lambda) \times (J_{light} - J_{dark})/P_i] \times 100 \qquad (2)$$

where λ is the wavelength of incident monochromatic light, J_{light} is the steady-state photocurrent density at given λ, J_{dark} is the dark current density and P_i is the power density of incident monochromatic light. Fig. 7B shows the IPCE spectra of Cu_2O and 3-layered MoS_2/Cu_2O photocathodes at ~0.2 V *vs*. RHE (−0.4 V *vs*. SCE) under frontside illumination. The figure also shows the absorbance data of Cu_2O, 3-layered MoS_2, and 3-layered MoS_2-modified Cu_2O. The IPCE spectra of Cu_2O and 3-layered MoS_2/Cu_2O photocathodes under backside illumination are shown in Fig. S14. Relative higher photocurrent response near short wavelength region for the frontside illumination than backside illumination is because of the efficient hole mobility when abundant excited states are produced at the electrode surface upon photoexcitation. Our study shows that MoS_2 modification improves the IPCE under both frontside and backside illuminations. The IPCE spectra reveal that MoS_2-modified Cu_2O sample shows a noticeably greater utilization of photons in the wavelength region of 400-600 nm compared to the unmodified Cu_2O sample because of the improved proton reduction kinetics in the presence of MoS_2. The higher absorbance for MoS_2-modified Cu_2O film is because of the additional absorption of MoS_2, which is a narrow band gap visible-light absorbing material (E_g=~1.8 eV) that typically shows absorption peaks in the visible range of 550-700 nm[55], as also seen from Fig. 7B. The IPCE of any device is closely associated with the photo-absorption ability of the photoactive layer. Electrodeposited Cu_2O films show an absorption peak at around ~500 nm. However, they are prone to defect formation as in ZnO, which results in deep-level defects such as oxygen vacancies or copper interstitials.[56, 57] These defects enable recombination of charge carriers that causes lower IPCE values. However, MoS_2 serves as a defect-passivating layer on Cu_2O, which to some extent lowers the charge carrier recombination in the visible region. Thus, higher IPCE of MoS_2/Cu_2O photocathode can be attributed to the visible light absorption in the higher wavelength spectral region and defect passivating ability of MoS_2. To further elucidate on the contributing factors toward the photocurrent enhancement, the EIS and MS measurements are performed. EIS analysis sheds light on the charge-transfer processes occurring at the electrolyte interface, while MS analysis

provides information about the nature and concentration of majority charge carriers as well as the built-in voltage of the system. Fig. 7C shows the Nyquist plots of Cu_2O and 3-layered MoS_2/Cu_2O electrodes obtained at −0.6 V Ag/AgCl (~0.0 V *vs*. RHE) in the dark and under frontside illumination. The Nyquist curves were fitted using an equivalent circuit comprised of a series resistance (R_s) and two RC (resistance and capacitance) circuits in parallel as shown in the figure inset. R_s is a sum of all the serial resistances consisting of the electrolyte, contact, electrode and cables. It is noteworthy that the Cu_2O/FTO electrode shows a higher R_s value (~420 Ω) than that of MoS_2/Cu_2O/FTO electrode (< 200 Ω). Additionally, the charge-transfer resistance (R_{ct}), typically the diameter of the semicircle, is inversely related to the photocurrent of the PEC system. The corresponding decrease in R_{ct} value with the addition of MoS_2 as a protecting layer (interfacial layer between Cu_2O and electrolyte) on Cu_2O/FTO, both in the dark as well under illumination, implies that charge carrier resistance at the photocathode-electrolyte interface is significantly improved. Under illumination, the R_{ct} value decreases considerably from 389 to 178 Ω after coating the MoS_2 layer onto Cu_2O. Trap resistance (R_{trap}) is one of the important parameters that reveals information about the defect sites in a material. The estimated R_{trap} values for Cu_2O in dark and illumination are 262 and 133 Ω, respectively. Upon MoS_2 coating on Cu_2O, these values were decreased considerably to 7.5 and 3.8 Ω, respectively. Thus defect states are passivated after MoS_2 modification of Cu_2O. This is an interesting result and more study is necessary because of the electrochemical behavior of Cu_2O depending on the applied potential and electrolyte. The MoS_2 coating not only protects the surface of Cu_2O electrode from reductive decomposition but also facilitates the charge transfer properties of Cu_2O, and hence actively contributes to photocurrent enhancement resulting from PEC water reduction. In other words, MoS_2 passivates the defect states, such as Cu vacancies in Cu_2O, additionally helping avoid the recombination of charge carriers. Thus, it can be established that MoS_2 at the interface promotes the effective shuttling of the charge carriers at the photocathode–electrolyte interface, which may be due to the formation of nanojunctions.[58] The interfacial space-charge capacitance (C_{sc}), which varies as a function of applied potential (V), primarily describes a photoelectrode/electrolyte interface that can be used to estimate the flat band potential and the majority carrier density of a semiconductor from the slope of the MS plot using Eq. (3):[59]

$$N_A = 2/(e_o\varepsilon\varepsilon_o\,|d(C_{sc}^{-2})/dV|) \quad (3)$$

where N_A is the acceptor density (hole density in *p*-type Cu_2O), e_o is the electron charge, ε_o is the permittivity of the vacuum, ε is the dielectric constant of the semiconductor (7.60 for Cu_2O). Fig. 7D shows the MS plots of the Cu_2O and 3-layered MoS_2/Cu_2O electrodes obtained at 1 kHz AC frequency in the dark. The negative slope of the MS plots confirms the *p*-type conductivity of Cu_2O electrodes. The N_A value decreases from 4.5×10^{19} cm^{-3} to 2.4×10^{19} cm^{-3} after coating MoS_2 on Cu_2O. This can understandably be attributed to the fact that *p*-type conductivity of electrodeposited Cu_2O originates primarily from defects, such as CuO vacancies. The defects or hole traps 0.40-0.55 eV above the top of the valence band maximum are verified in Cu_2O. by deep level transient spectroscopy,[57] which are attributed to structural anomalies such as CuO islands.[60] Such defects are passivated after surface coating with MoS_2, resulting in reduced hole densities. Similar N_A values are reported in the literature for pristine and protected Cu_2O electrodes.[61, 62] The extrapolated straight portion of the MS plot on the x-axis at C_{sc}=0 gives the flat band potential (E_{fb}) of the material, which is typically close to the onset potential in the photocurrent response. The E_{fb} values are close to the onset potentials of Cu_2O and MoS_2/Cu_2O as seen in Fig. 7A. No noticeable change in E_{fb} is observed after MoS_2 coating. The E_{fb} value for both the Cu_2O and MoS_2/Cu_2O electrodes is 0.63 ± 0.005 V *vs*. RHE, which is in line with the reported values.[59, 62]

Fig. 8A shows the photographs of as-grown Cu_2O and N_2-annealed MoS_2-modified Cu_2O photocathodes with different numbers of spin-coated layers, both before and after the PEC measurement. It is evident that the color of the Cu_2O film area performing the water reduction reaction is unchanged after PEC measurement with increasing number of spin-coated layers of

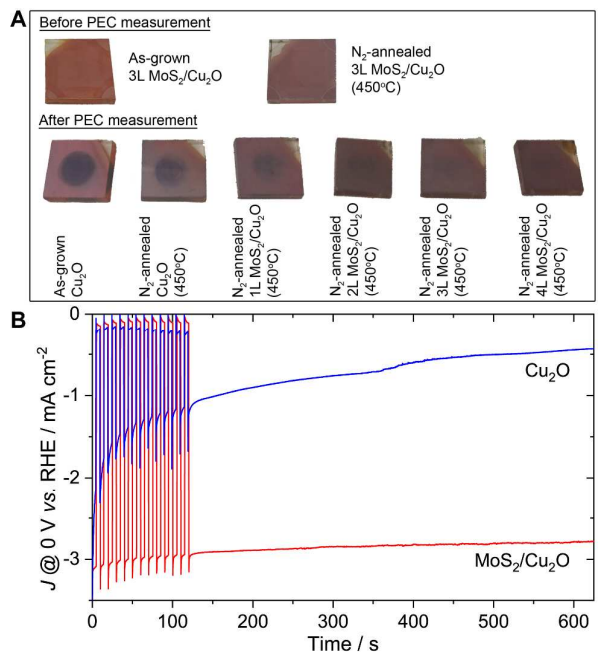

Fig. 8 (A) Photographs of as-grown Cu_2O and N_2-annealed MoS_2-modified Cu_2O samples before and after the PEC measurements. The color change from reddish brown to black indicates reductive photodecomposition of Cu_2O to Cu/CuO. (B) Chronoamperometric responses of as-grown Cu_2O and MoS_2-modified Cu_2O photocathodes at an applied potential of 0 V vs. RHE in 0.1 M phosphate buffered (pH 7) 0.5 M Na_2SO_4 electrolyte.

MoS_2. In other words, the MoS_2 layer passivates the reductive photo-decomposition of Cu_2O to Cu or/and CuO and protects the chemical state of the electrode, resulting in improved PEC water reduction performance. Fig. 8B shows the current transient responses of as-grown Cu_2O and MoS_2-modified Cu_2O electrodes recorded with chopped and steady 1 sun light illumination in a buffered 0.5 M Na_2SO_4 electrolyte at a

constant potential of −0.6 V *vs.* SCE (0 V vs. RHE). The photocurrent of Cu_2O degrades rapidly in first two min and gradually decreases further. The percentage decrease of photocurrent for Cu_2O and MoS_2-modified Cu_2O electrodes after 10 min is 77 and 9%, respectively. Thus, MoS_2-modified Cu_2O is about 8 times more stable than pristine Cu_2O, suggesting that MoS_2 protects Cu_2O from photo-corrosion making it more durable. With a new set of samples, the long-term photostability tests under 1 sun illumination are performed for 1 h in the same buffered electrolyte as shown in Fig. S15. At the end of the stability test, the light was chopped ON and OFF to observe the light and dark responses of the photocathodes. It is clear that MoS_2-modified Cu_2O is relatively more stable than the as-grown Cu_2O photocathode. As-grown Cu_2O shows huge dark current with declined photocurrent at the end of 1 h stability test whereas MoS_2-modified Cu_2O still shows negligibly small dark current with appreciable photocurrent. The net photocurrent density for as-grown Cu_2O photoelectrode waned down from initial 2.1 to 0.1 mA cm^{-2} after 1h illumination whereas it decreased from 3.2 to 1.7 mA cm^{-2} for MoS_2-modified Cu_2O photoelectrode. At the end of stability test, the color of as-grown Cu_2O turned slightly black unlike MoS_2-modified Cu_2O as shown in the inset of the figure. The photogenerated electrons tend to reduce the unprotected Cu_2O into Cu and photogenerated holes tend to oxidize Cu_2O into CuO (turning the illuminated area black). Fig. S16 shows the XRD patterns of as-grown Cu_2O and N_2-annealed MoS_2-modified Cu_2O after 1 h stability test. The as-grown Cu_2O underwent electrochemical transformation by partially reducing Cu_2O to Cu as two prominent metallic Cu peaks emerge at 50.55 and 59.11°. The reduction of Cu_2O to Cu in MoS_2-modified Cu_2O is less and its XRD pattern after 1 h stability test shows a tiny peak centered at 50.55°. Furthermore, the surface morphologies of as-grown Cu_2O and MoS_2-modified Cu_2O samples before and after the 1 h photostability tests are monitored as shown in Fig. S17. After 1 h illumination, the sharp-edged pyramidal grains of as-grown Cu_2O are broken down into nanoparticles. Additionally, the grain boundaries are opened allowing the electrolyte to leak to the back contact, consequently yielding an increase in dark current as seen from the stability curve. On the other hand, MoS_2-modified Cu_2O undergoes relatively less damage with regard to the grain and the grain boundaries although there is some loss of the top layer of the electrode. This observation suggests that the Cu_2O maintained its oxidized state upon MoS_2-modification even after 1 h stability test.

Since XRD studies did not reveal any information about the molybdenum sulfide phase on Cu_2O, we performed HRTEM analysis on the N_2-annealed MoS_2-modified Cu_2O sample. Fig. 9A and 9B show the corresponding HRTEM images of Cu_2O and MoS_2 along with the selected area electron diffraction (SAED) pattern for molybdenum sulfide. The close match of lattice parameters 0.294 nm (110), 0.212 nm (200), and 0.245 nm (111) with those of Cu_2O,[63] and 0.270 nm (100) with that of MoS_2 confirmed the formation of MoS_2 on Cu_2O electrode.

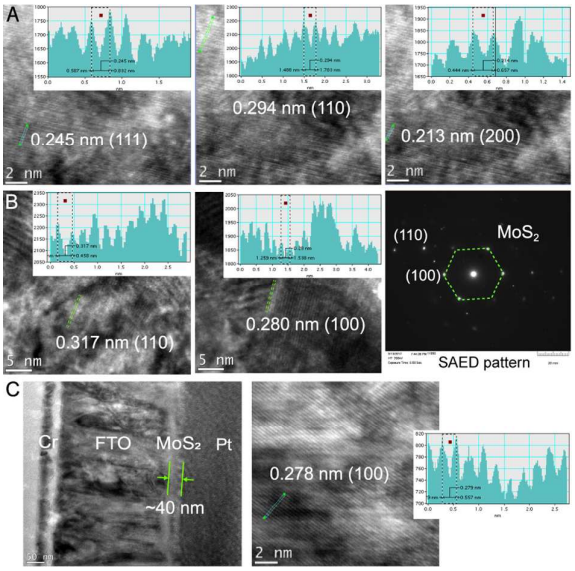

Fig. 9 (A, B) HRTEM images of N_2-annealed 3-layered MoS_2-modified Cu_2O with selected area electron diffraction (SAED) pattern for MoS_2. (C) Bright field cross-section TEM and HRTEM images of MoS_2 coated on FTO.

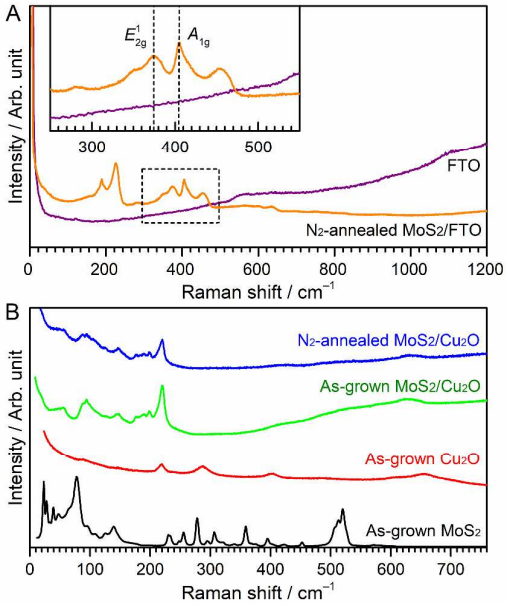

Fig. 10 Raman spectra of (A) FTO and N_2-annealed MoS_2/FTO, (B) as-grown MoS_2, as-grown Cu_2O, as-grown MoS_2/Cu_2O, and N_2-annealed MoS_2/Cu_2O samples.

Additionally, the crystallinity of the pristine MoS_2 is further characterized by SAED/FFT patterns. The FFT pattern of MoS_2 with bright spots denotes highly crystalline property and indexes to MoS_2.[64] To determine the thickness of the MoS_2 layer, the MoS_2 film was alternatively fabricated onto FTO under identical conditions and FIB-TEM analysis was performed. Figure 9B shows a bright field TEM image of MoS_2/FTO specimen with a platinum cap. The film thickness of 3-layered MoS_2 obtained from the cross-sectional TEM is ~30-40 nm.

Raman spectroscopy is a valuable technique for the identification and characterization of phonon vibrational modes of chemical bonds. Fig. 10A shows the Raman spectra of bare FTO and MoS_2/FTO samples annealed at 450°C in N_2. As evident from the figure, dominant optical modes are observed mainly at 380 cm^{-1} and 405 cm^{-1}, which correspond to the Raman-active in-plane (E_{2g}) and out-of-plane (A_{1g}) modes of MoS_2, respectively. The E_{2g} mode is sensitive to strain, while the A_{1g} mode shows a weak strain dependence.[65] The subtle changes in Raman spectra (minor variations in peak intensity or position) indicate the presence of electronic doping or strain effects.[66] These Raman-active modes are apparently not seen in the as-grown and N_2-annealed MoS_2/Cu_2O/FTO samples (Fig. 10B) possibly due to the dominance of signals from Cu_2O itself. Collectively, the improved PEC performance by MoS_2-modified Cu_2O photocathode is attributed to the photocatalytically active polyhedral crystalline morphology of Cu_2O, the enhanced absorptivity in the visible region, the facilitated separation of electron-hole pairs and the reduced carrier recombination because of decreased interface defects/hole traps in the presence of MoS_2.

Conclusions

In summary, we have demonstrated a MoS_2-coating technique to obtain stable and efficient copper-oxide-based photocathode materials for PEC hydrogen production. The photocorrosion problem associated with electrodeposited *p*-type Cu_2O photocathode is addressed by spin-coating a thin ~40 nm MoS_2 layer onto the surface using a novel MoS_2 precursor complex. The MoS_2 coating not only prevents the reductive photodecomposition of Cu_2O to Cu but also enhances the overall PEC activity of the photocathode. The catalytic activity of MoS_2 using such complex precursors can readily be tuned by controlling the number of spin-coated layers and the annealing temperature in the N_2 atmosphere. Additionally, the action spectra indicate that the MoS_2 coating helps improve the light absorptivity by Cu_2O in the visible region. Electrochemical impedance spectroscopy measurements of MoS_2-modified Cu_2O suggests improvements in interface properties that lead to enhanced separation of electron-hole pairs as well as reduced carrier recombination because of a decrease in interfacial defects or hole traps. The MoS_2-modified Cu_2O photocathodes exhibit photocurrent densities as high as 6.5 mA cm^{-2} at −0.2 V *vs*. RHE in 0.5 M Na_2SO_4 electrolyte under standard 1 sun illumination conditions, which make them potential candidates for a self-assisted hybrid water splitting system for hydrogen fuel generation. Further work is needed to improve the stability of Cu_2O photocathode in relatively lower pH media. This work highlights the promise of spin-coatable molybdenum disulfide as a catalytically active thin-film passivation layer for several other unstable semiconductor water-splitting materials. We also envisage that such *p*-type photocathode system can be combined with an *n*-type photoanode system to establish a cost-effective and efficient unassisted PEC water splitting system to produce hydrogen fuel.

Conflicts of interest

There are no conflicts to declare.

Acknowledgments

We acknowledge the support of National Science Foundation (NSF) under award numbers OIA-1539035 and CHE-1508192. The authors are also thankful for the support from the University of Alabama through the RGC-level 2 award and to Prof. Mark Weaver's group for TGA/DSC measurements. PS thanks Yanxiao Ma for partial support of SEM imaging. We appreciate valuable discussions with Prof. Russ Schmehl of Tulane University.

Notes and references

1. N. S. Lewis, *Sci.*, 2016, **351**, aad1920.
2. M. R. Shaner, H. A. Atwater, N. S. Lewis and E. W. McFarland, *Energy Environ. Sci.*, 2016, **9**, 2354-2371.
3. J. M. Thomas and K. D. M. Harris, *Energy Environ. Sci.*, 2016, **9**, 687-708.
4. M. Crespo-Quesada and E. Reisner, *Energy Environ. Sci.*, 2017, **10**, 1116-1127.
5. C. Jiang, S. J. A. Moniz, A. Wang, T. Zhang and J. Tang, *Chem. Soc. Rev.*, 2017, **46**, 4645-4660.
6. K. Sun, I. A. Moreno-Hernandez, W. C. Schmidt, X. Zhou, J. C. Crompton, R. Liu, F. H. Saadi, Y. Chen, K. M. Papadantonakis and N. S. Lewis, *Energy Environ. Sci.*, 2017, **10**, 987-1002.
7. R. H. Coridan, A. C. Nielander, S. A. Francis, M. T. McDowell, V. Dix, S. M. Chatman and N. S. Lewis, *Energy Environ. Sci.*, 2015, **8**, 2886-2901.
8. R. Sathre, J. B. Greenblatt, K. Walczak, I. D. Sharp, J. C. Stevens, J. W. Ager and F. A. Houle, *Energy Environ. Sci.*, 2016, **9**, 803-819.
9. P. Bornoz, F. F. Abdi, S. D. Tilley, B. Dam, R. van de Krol, M. Graetzel and K. Sivula, *J. Phys. Chem. C*, 2014, **118**, 16959-16966.
10. M. S. Prévot and K. Sivula, *J. Phys. Chem. C*, 2013, **117**, 17879-17893.
11. S. J. A. Moniz, S. A. Shevlin, D. J. Martin, Z.-X. Guo and J. Tang, *Energy Environ. Sci.*, 2015, **8**, 731-759.
12. X. An, Y. Wang, J. Lin, J. Shen, Z. Zhang and X. Wang, *Sci. Bull.*, 2017, **62**, 599-601.
13. A. Paracchino, V. Laporte, K. Sivula, M. Grätzel and E. Thimsen, *Nat. Mater.*, 2011, **10**, 456-461.
14. Y. Zhang, B. Deng, T. Zhang, D. Gao and A.-W. Xu, *J. Phys. Chem. C*, 2010, **114**, 5073-5079.
15. L. Pan, J.-J. Zou, T. Zhang, S. Wang, Z. Li, L. Wang and X. Zhang, *J. Phys. Chem. C*, 2014, **118**, 16335-16343.
16. T. D. Golden, M. G. Shumsky, Y. Zhou, R. A. VanderWerf, R. A. Van Leeuwen and J. A. Switzer, *Chem. Mater.*, 1996, **8**, 2499-2504.
17. L. C. Olsen, F. W. Addis and W. Miller, *Solar Cells*, 1982, **7**, 247-279.

18. A. O. Musa, T. Akomolafe and M. J. Carter, *Sol. Energy Mater. Sol. Cells*, 1998, **51**, 305-316.
19. S. Chatterjee and A. J. Pal, *J. Phys. Chem. C*, 2016, **120**, 1428-1437.
20. M.-K. Son, L. Steier, M. Schreier, M. T. Mayer, J. Luo and M. Gratzel, *Energy Environ. Sci.*, 2017, **10**, 912-918.
21. J. Azevedo, L. Steier, P. Dias, M. Stefik, C. T. Sousa, J. P. Araújo, A. Mendes, M. Graetzel and S. D. Tilley, *Energy Environ. Sci.*, 2014, **7**, 4044-4052.
22. C. G. Morales-Guio, S. D. Tilley, H. Vrubel, M. Grätzel and X. Hu, *Nat. Commun.*, 2014, **5**, 3059.
23. C. Li, T. Hisatomi, O. Watanabe, M. Nakabayashi, N. Shibata, K. Domen and J.-J. Delaunay, *Energy Environ. Sci.*, 2015, **8**, 1493-1500.
24. A. A. Dubale, W.-N. Su, A. G. Tamirat, C.-J. Pan, B. A. Aragaw, H.-M. Chen, C.-H. Chen and B.-J. Hwang, *J. Mater. Chem. A*, 2014, **2**, 18383-18397.
25. C. Yang, P. D. Tran, P. P. Boix, P. S. Bassi, N. Yantara, L. H. Wong and J. Barber, *Nanoscale*, 2014, **6**, 6506-6510.
26. H. Qi, J. Wolfe, D. Fichou and Z. Chen, *Sci. Rep.*, 2016, **6**, 30882.
27. N. M. Latiff, L. Wang, C. C. Mayorga-Martinez, Z. Sofer, A. C. Fisherc and M. Pumera, *Nanoscale*, 2016, **8**, 16752-16760.
28. J. Yang and H. S. Shin, *J. Mater. Chem. A*, 2014, **2**, 5979-5985.
29. Z. L. He and W. X. Que, *Appl. Mater. Today*, 2016, **3**, 23-56.
30. P. C. K. Vesborg, B. Seger and I. Chorkendorff, *J. Phys. Chem. Lett.*, 2015, **6**, 951-957.
31. D. Voiry, H. Yamaguchi, J. W. Li, R. Silva, D. C. B. Alves, T. Fujita, M. W. Chen, T. Asefa, V. B. Shenoy, G. Eda and M. Chhowalla, *Nat. Mater.*, 2013, **12**, 850-855.
32. B. Hinnemann, P. G. Moses, J. Bonde, K. P. Jørgensen, J. H. Nielsen, S. Horch, I. Chorkendorff and J. K. Nørskov, *J. Am. Chem. Soc.*, 2005, **127**, 5308-5309.
33. J. Hu, B. Huang, C. Zhang, Z. Wang, Y. An, D. Zhou, H. Lin, M. K. H. Leung and S. Yang, *Energy Environ. Sci.*, 2017, **10**, 593-603.
34. K. C. Kwon, S. Choi, K. Hong, C. W. Moon, Y.-S. Shim, D. H. Kim, T. Kim, W. Sohn, J.-M. Jeon, C.-H. Lee, K. T. Nam, S. Han, S. Y. Kim and H. W. Jang, *Energy Environ. Sci.*, 2016, **9**, 2240-2248.
35. L. Zhang, Y. Li, C. Li, Q. Chen, Z. Zhen, X. Jiang, M. Zhong, F. Zhang and H. Zhu, *ACS Nano*, 2017, **11**, 12753-12763.
36. X. Yu, N. Guijarro, M. Johnson and K. Sivula, *Nano Lett.*, 2018, **18**, 215-222.
37. A. Müller, R. G. Bhattacharyya and B. Pfefferkorn, *Chem. Ber.*, 1979, **112**, 778-780.
38. H. Zimmermann, K. Hegetschweiler, T. Keller, V. Gramlich, H. W. Schmalle, W. Petter and W. Schneider, *Inorg. Chem.*, 1991, **30**, 4336-4341.
39. J. W. McDonald, G. D. Friesen, L. D. Rosenhein and W. E. Newton, *Inorg. Chim. Acta*, 1983, **72**, 205-210.
40. M. J. Mayor-López, J. Weber, K. Hegetschweiler, M. D. Meienberger, F. Joho, S. Leoni, R. Nesper, G. J. Reiss, W. Frank, B. A. Kolesov, V. P. Fedin and V. E. Fedorov, *Inorg. Chem.*, 1998, **37**, 2633-2644.
41. E. A. Il'inchik, T. M. Polyanskaya and K. G. Myakishev, *Russ. J. Gen. Chem.*, 2007, **77**, 1148-1154.
42. E. A. Il'inchik, T. M. Polyanskaya, K. G. Myakishev, T. V. Basova and B. A. Kolesov, *Russ. J. Gen. Chem.*, 2002, **72**, 1862-1866.
43. V. P. Fedin, M. N. Sokolov, O. A. Geras'ko, A. V. Virovets, N. V. Podberezskaya and V. Y. Fedorov, *Inorg. Chim. Acta*, 1992, **192**, 153-156.
44. M. D. Meienberger, K. Hegetschweiler, H. Rüegger and V. Gramlich, *Inorg. Chim. Acta*, 1993, **213**, 157-169.
45. H.-P. Zhu, C.-N. Chen, Q.-T. Liu and J.-T. Chen, *Acta Crystallogr. Sect. C*, 1998, **54**, 1273-1275.
46. V. P. Fedin, M. N. Sokolov, A. V. Virovets, N. V. Podberezskaya and V. Ye. Fedorov, *Inorg. Chim. Acta*, 1992, **194**, 195-200.
47. A. Kay, I. Cesar and M. Grätzel, *J. Am. Chem. Soc.*, 2006, **128**, 15714-15721.
48. G. Zhang, H. Liu, J. Qu and J. Li, *Energy Environ. Sci.*, 2016, **9**, 1190-1209.
49. S. J. Rowley-Neale, J. M. Fearn, D. A. C. Brownson, G. C. Smith, X. Ji and C. E. Banks, *Nanoscale*, 2016, **8**, 14767-14777.
50. X. Huang, Z. Zeng, S. Bao, M. Wang, X. Qi, Z. Fan and H. Zhang, *Nat. Commun.*, 2013, **4**, 1444.
51. T. F. Jaramillo, K. P. Jørgensen, J. Bonde, J. H. Nielsen, S. Horch and I. Chorkendorff, *Sci.*, 2007, **317**, 100-102.
52. M.-R. Gao, J.-X. Liang, Y.-R. Zheng, Y.-F. Xu, J. Jiang, Q. Gao, J. Li and S.-H. Yu, *Nat. Commun.*, 2015, **6**, 5982.
53. B. E. Conway and B. V. Tilak, *Electrochim. Acta*, 2002, **47**, 3571-3594.
54. Y. Li, H. Wang, L. Xie, Y. Liang, G. Hong and H. Dai, *J Am. Chem. Soc.*, 2011, **133**, 7296-7299.
55. Y. Lee, J. Lee, H. Bark, I.-K. Oh, G. H. Ryu, Z. Lee, H. Kim, J. H. Cho, J.-H. Ahn and C. Lee, *Nanoscale*, 2014, **6**, 2821-2826.
56. S. Laidoudi, A. Y. Bioud, A. Azizi, G. Schmerber, J. Bartringer, S. Barre and A. Dinia, *Sem. Sci. Technol.*, 2013, **28**, 115005.
57. G. K. Paul, Y. Nawa, H. Sato, T. Sakurai and K. Akimoto, *Appl. Phys. Lett.*, 2006, **88**, 141901.
58. A. Mahmood, F. Tezcan and G. Kardaş, *J. Mater. Sci.*, 2017, **28**, 12937-12943.
59. Y. Yang, D. Xu, Q. Wu and P. Diao, *Sci. Rep.*, 2016, **6**, 35158.
60. D. O. Scanlon, B. J. Morgan and G. W. Watson, *J. Chem. Phys.*, 2009, **131**, 124703.
61. J. Choi, J. T. Song, H. S. Jang, M.-J. Choi, D. M. Sim, S. Yim, H. Lim, Y. S. Jung and J. Oh, *Electron. Mater. Lett.*, 2017, **13**, 57-65.
62. Z. Zhang and P. Wang, *J. Mater. Chem.*, 2012, **22**, 2456-2464.
63. J. G. Lee, D.-Y. Kim, J.-H. Lee, M.-w. Kim, S. An, H. S. Jo, C. Nervi, S. S. Al-Deyab, M. T. Swihart and S. S. Yoon, *ACS Appl. Mater. Interfaces*, 2016, **8**, 15406-15414.
64. H. Li, K. Yu, C. Li, Z. Tang, B. Guo, X. Lei, H. Fu and Z. Zhu, *Sci. Rep.*, 2015, **5**, 18730.
65. C. Rice, R. J. Young, R. Zan, U. Bangert, D. Wolverson, T. Georgiou, R. Jalil and K. S. Novoselov, *Phys. Rev. B*, 2013, **87**, 081307.
66. A. Castellanos-Gomez, R. Roldán, E. Cappelluti, M. Buscema, F. Guinea, H. S. J. van der Zant and G. A. Steele, *Nano Lett.*, 2013, **13**, 5361-5366.